



OPEN Effect of substrate temperature on properties of WS_2 thin films

Monireh Jafari¹, Mohammad Mahdi Shahidi² & Mohammad Hossein Ehsani¹✉

The WS_2 thin films were deposited on glass substrates with RF magnetron sputtering using a WS_2 target to study the effect of substrate temperature (25, 100, 200, and 300 °C) on their properties. In this study, we investigated the morphological, structural, and optical characteristics of the films. FESEM images show that all the samples consist of nanoparticles, with the exception of the film deposited at 200 °C, which uniquely exhibited a nanosheet morphology. The AFM spectrum of the samples determined that the sample with a substrate temperature of 200 °C had the highest roughness, which confirms the results obtained from the FESEM images of the samples. The XRD patterns of all the thin films showed the preferred orientation (104) related to the WS_2 phase, and among the samples, the film deposited at 200 °C exhibited the largest crystallite size and the lowest strains. Also, no additional peak related to the oxide phase was observed in XRD and Raman spectra. The band gap of the 200 °C sample was lower than the other samples, and because it has a larger crystal size, this can be caused by quantum confinement. At 200 °C, the resistivity reached its highest value, accompanied by a significant decrease in carrier mobility and concentration, likely due to structural disorder and increased porosity in this sample.

Keywords WS_2 , Thin film, Sputtering, Substrate temperature

Recent studies on various nanostructured thin films have shown that factors such as substrate temperature and synthesis method significantly affect their morphological, optical, and structural properties¹. Building on these insights, tungsten disulfide (WS_2) has attracted increasing attention due to its layered structure and promising optical and electronic characteristics for optoelectronic applications^{2–4}. Among the applications of WS_2 , we can mention gas sensors and photodetectors^{5,6}. WS_2 is a semiconductor with a direct band gap in bulk mode and an indirect band gap in monolayer mode⁷. The synthesis of WS_2 nanostructures can significantly affect their structural integrity and optical characteristics. There are various physical and chemical methods such as chemical vapor deposition (CVD)^{8,9}, magnetron sputtering^{10,11}, chemical bath deposition (CBD)^{12,13}, and hydrothermal methods^{14,15} for the synthesis of this material. Among these synthesis methods, sputtering can be a suitable candidate, controlling many parameters to attain pure and resistant thin films with high crystallinity and quality^{16,17}. This method allows for precise control over the deposition parameters, such as synthesis time, substrate temperature, target-to-substrate distance, gas flow rate, input gas, and working pressure^{18,19}. Substrate temperature has been identified as a key parameter influencing the crystallinity, morphology, and optical performance of WS_2 films²⁰. In particular, the appropriate thermal energy on the surface of the substrate increases the mobility of the adatoms, which move to the proper atomic position, thereby increasing the crystallinity¹⁸. Exploring the effect of substrate temperature on WS_2 nanostructures can help to optimize their synthesis processes, leading to enhanced performance in practical applications. Only a few reports have been presented on the effect of temperature on sputtering WS_2 layers. Genut et al.²¹ synthesized tungsten thin films (about 50 nm thick) by a sputtering method on various molybdenum, tungsten, quartz, and glass slides. For this purpose, the samples were annealed in a quartz furnace with H_2S flow in the temperature range of 400 to 1000 °C, and the effect of the substrate at these temperatures on the WS_2 layers was investigated. Ye et al.²² investigated the effect of annealing temperature on the properties of WS_2 thin films by sputtering on glass and silicon substrates. For this purpose, thin WS_2 layers with a thickness of 300 nm were synthesized by RF magnetic sputtering using a WS_2 target, and finally, the samples were annealed in a nitrogen atmosphere at different temperatures of 200, 300, 400, and 500 °C for 1 h. Ma et al.²³ investigated the effects of DC sputtering power and rapid thermal processing temperature on WS_2 thin films. The layers were synthesized in a sputtering machine using a WS_2 target at different powers of 80, 120, and 160 W. The prepared layers were annealed in a rapid thermal processing system, where the temperature increased from 200 °C to 800 °C at a rate of 3 °C/s. However,

¹Faculty of Physics, Semnan University, Semnan, Iran. ²UNESCO-UNISA-ITL/NRF Africa Chair in Nanoscience and Nanotechnology (U2ACN2), College of Graduate Studies, University of South Africa (UNISA), P.O. Box 392, Muckleneuk Ridge, Pretoria, South Africa. ✉email: mmahdishahidi@gmail.com; ehsani@semnan.ac.ir

the effect of substrate temperature during synthesis on this material by the RF magnetron sputtering method has not been widely investigated yet.

In this study, we investigated how the substrate temperature during synthesis affects the morphology, structural and optical properties of WS_2 nanostructures synthesized using the RF magnetron sputtering technique in the presence of argon gas. This study aims to systematically investigate WS_2 thin films through techniques such as FESEM, AFM, XRD, Raman, and UV-Vis. spectroscopy.

Experimental

WS_2 thin films were deposited using the RF sputtering technique with a WS_2 target of 99.99% purity, 2 inches in diameter, and 75 W power in an argon atmosphere. Prior to deposition, the glass substrates were under a cleaning process involving soap and water, followed by ethanol, acetone, and distilled water in an ultrasonic device for 20 min. After cleaning, the substrates were dried with an air pump. The cleaned substrates were then placed into the sputtering chamber, where the base pressure and working pressure were maintained at 8.5×10^{-5} and 7×10^{-3} Torr, respectively. The deposition rate was approximately 2 Å/s and the film thickness was uniformly set at 200 nm, which was controlled by a quartz crystal in the sputtering system. To investigate the influence of substrate temperature, four different temperatures (25, 100, 200, and 300 °C) were applied during deposition. The synthesis process parameters are listed in Table 1.

The surface morphology of the fabricated thin films was examined using a Zeiss Sigma 300-HV field emission scanning electron microscope (FESEM) and an Atomic Force Microscope (AFM). The crystalline structures were characterized by Grazing Incidence X-Ray Diffraction (GIXRD; Bruker AXS) with $CuK\alpha$ radiation (1.5418 Å). Additionally, Micro-Raman spectroscopy (Avantes 532-Ci) was employed for further structural analysis, using an excitation wavelength of 532 nm. The optical properties of the films were estimated with a Shimadzu UV-1800 ultraviolet-visible (UV-Vis) spectrophotometer through the wavelength range of 300–1100 nm. The electrical properties were evaluated using an ECOPIA Hall effect measurement system, employing the van der Pauw four-probe configuration.

Results and discussions

Surface morphology

Figure 1 shows the FESEM images of WS_2 samples at 100 and 200 nm scales. These high-resolution images present the morphological changes of WS_2 nanostructures at different substrate temperatures. Increasing the temperature of the substrate to 100 °C results in a growth in the size of the nanoparticles. As the substrate temperature reaches 200 °C, a significant transformation takes place, resulting in the formation of nanosheets. These images suggest a change in the growth mechanism, where higher substrate temperatures promote lateral growth and thus sheet-like structures. The formation of nanosheets is significant due to their high surface-to-volume ratio and their performance in various applications. Upon reaching a temperature of 300 °C, the WS_2 films exhibit separated grains on the surface. As the temperature rises, the energy levels of the adatoms arriving at the surface increase significantly, leading to greater atomic mobility²⁴. Due to the shadowing effect, particles can be absorbed by higher surface points (hills), or, due to the re-emission effect, particles can “bounce around” before settling in the correct places on the surface^{25,26} which could have happened for the T300 sample. The images displayed on the right show cross-sectional views, where the thickness of all layers is uniformly 200 nm.

Figure 2 shows 3D atomic force microscopy (AFM) micrographs of the surface of all samples at a scale of 5 $\mu\text{m} \times 5 \mu\text{m}$. As seen in the pictures, there are small crystal particles in samples T25 and T100. In contrast, the T200 sample shows a different surface morphology with the presence of larger crystal particles. As the substrate temperature increases to 300 °C (T300), it shows grains that are spaced apart.

The average roughness (R_a) and root mean square roughness (R_q) values were calculated using the following Eqs^{27,28}:

$$R_a = \frac{1}{n} \sum y_i \quad (1)$$

$$R_q = \sqrt{\frac{1}{n} \sum y_i^2} \quad (2)$$

Here y_i represents the analyzed surface profile, and n is the evaluation length. The results of the roughness measurements are summarized in Table 2. The roughness of the T200 sample is higher than that of the other samples, and the FESEM images suggest that this sample consists of nanosheet-like structures, indicating increased porosity. These observations were further supported by AFM analysis. While the combination of FESEM and

Parameters	Value
Base pressure	8.5×10^{-5} Torr
Working pressure	7×10^{-3} Torr
RF power	75 w
Argon gas flow	10 SCCM
Substrate temperature	25, 100, 200, 300 °C

Table 1. Parameters and their respective values for the deposition of WS_2 thin films.

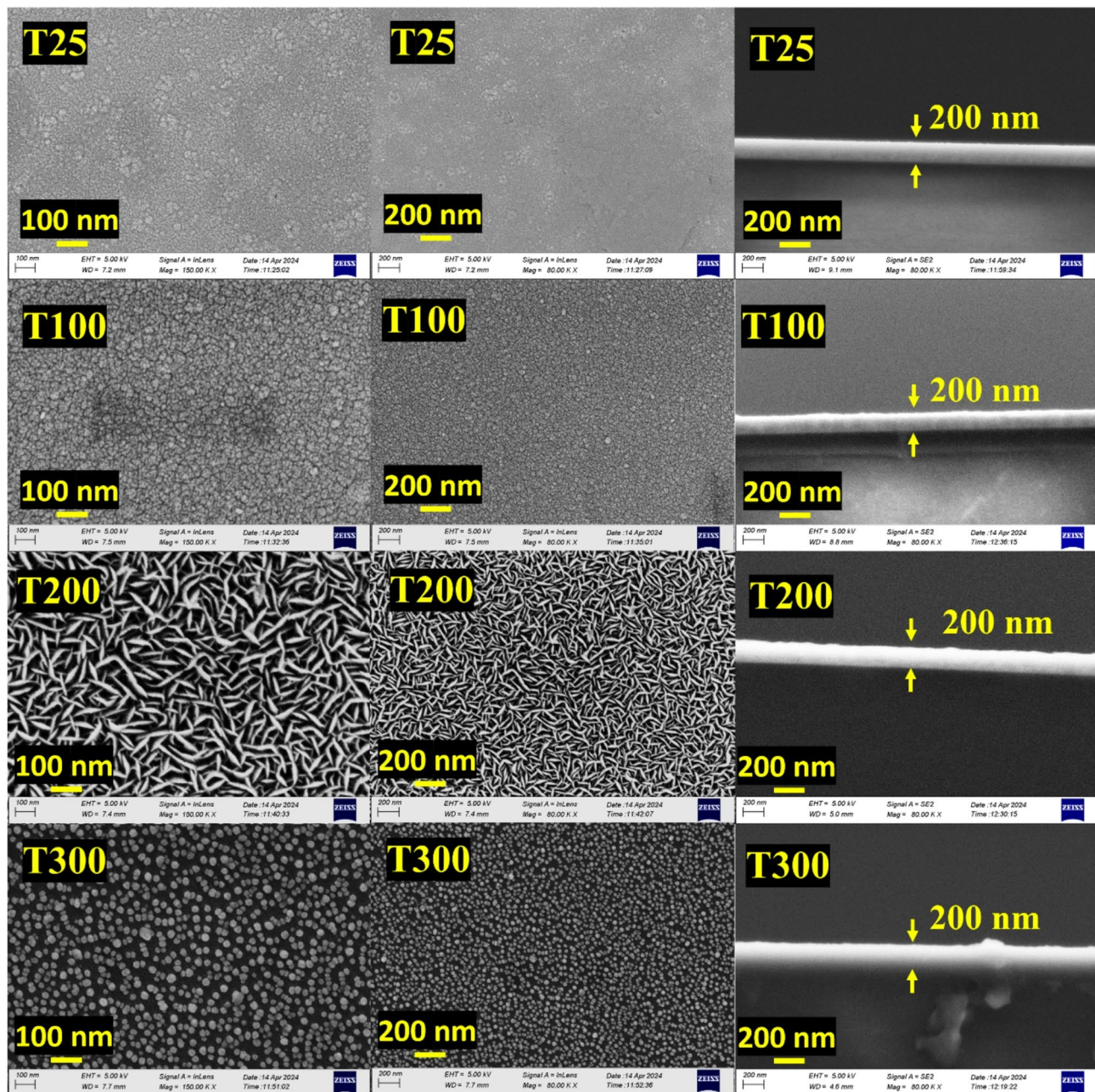


Fig. 1. Top and cross-sectional FESEM images of WS_2 thin films deposited at various temperatures by sputtering method.

AFM data points toward a distinct morphological evolution at this temperature, further investigations would be beneficial to confirm the detailed structural nature. In particular, at 300 °C, although the surface roughness is relatively high (about 5.5 nm), other structural changes, such as defect density, grain boundaries, and possible phase transitions, may lead to increased phonon scattering and non-radiative recombination, which could reduce the effective phonon lifetime²⁹.

Structural properties

Figure 3 (a and b) present the XRD diffractogram and the Raman shift spectrum of the studied samples. According to the XRD spectrum of samples (Fig. 3a), it can be seen that the peaks (104), (009), (110), and (116) are related to the hexagonal phase of WS_2 (JCPDS Card No. 35-0651). Also, no additional peaks related to oxide phases are observed. Among the peaks, the peak (104) is considered as the preferred peak. As the temperature increases from 25 °C to 100 °C and then 200 °C, an increase in peak intensity is observed, while the temperature reaches 300 °C, a decrease in peak intensity is observed again. Among the samples, sample T200 has sharper peaks. The sharpness of these peaks indicates a higher degree of crystallinity of the substance³⁰. These observations show that the T200 sample has been subjected to optimal growth conditions, resulting in better crystallinity compared

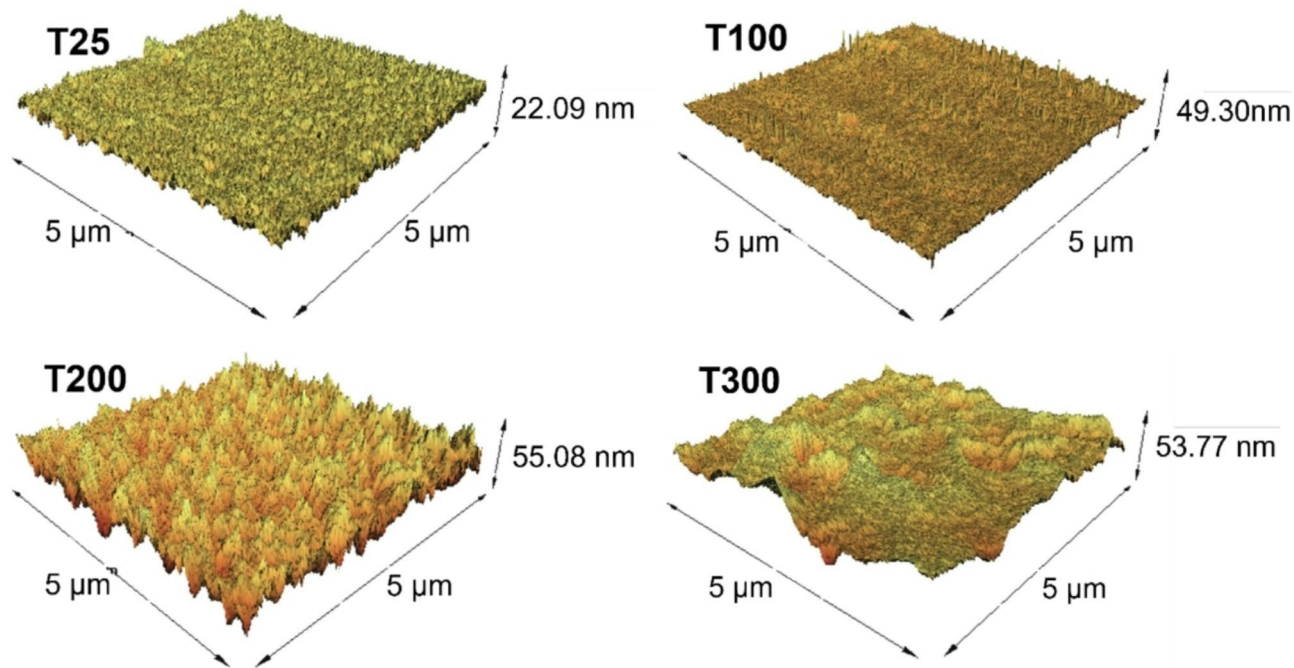


Fig. 2. Topographic images (3D) obtained by AFM for WS_2 thin films prepared at various substrate temperatures by magnetron sputtering.

Samples	R_a (μm)	R_q (nm)
T25	0.0041	1.12
T100	0.617	2.17
T200	0.719	6.01
T300	0.432	5.58

Table 2. The roughness values for all samples WS_2 .

to other samples. According to Table 3, a slight change can be seen in the peaks corresponding to the WS_2 films synthesized at different substrate temperatures, which can be caused by the expansion or contraction of the crystal lattice^{11,31}.

To obtain a more detailed evaluation of the structural properties, we calculated the crystal size (D) using Scherer's equation, along with the dislocation density (δ) and the micro-strain (ϵ) values, from the following relations^{32–34}:

$$D = 0.9\lambda / \beta \cos\theta \quad (3)$$

$$\delta = 1/D^2 \quad (4)$$

$$\epsilon = \beta \cos\theta / 4 \quad (5)$$

Where θ is the Bragg angle, β (in radians) is the full width at half maximum (FWHM), and λ is the wavelength of X-ray radiation. The results of the calculations are given in Table 3. According to these analyses among the samples, sample T200 has the largest crystal size and the lowest density of dislocations and crystal strains among the samples. A lower dislocation density results in fewer defects within the crystal lattice, potentially enhancing the material's electrical and optical properties. Furthermore, reduced crystal micro-strain provides improved stability and performance in various applications.

For further structural analysis of the samples, Raman spectroscopy was employed (Fig. 3b). The clear observation of Raman peaks indicates the good quality of the samples. The two peaks observed at 349 and 416 cm^{-1} correspond to the E_{2g}^1 and A_{1g} modes, indicating in-plane and out-of-plane vibrations, respectively. Specifically, the two peaks at 349 and 416 cm^{-1} correspond to the E_{2g}^1 and A_{1g} modes, which represent in-plane and out-of-plane vibrations, respectively^{10,35}. Understanding vibrational modes is crucial for the structural analysis of materials and phonon interactions.

To calculate the phonon lifetime, we have calculated from the energy-time uncertainty relationship^{36,37}:

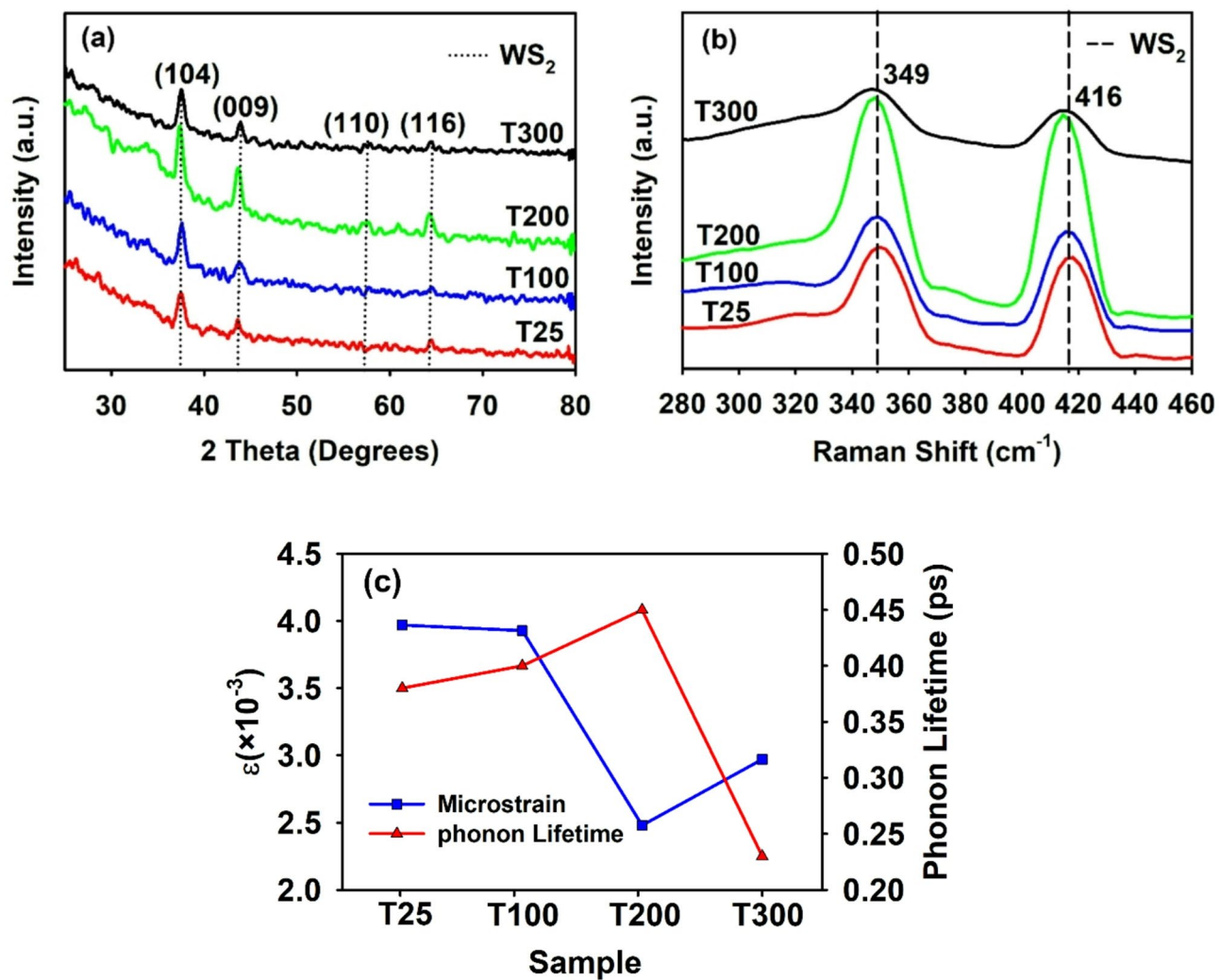


Fig. 3. (a) XRD patterns and (b) Raman spectra of WS₂ deposited on various substrate temperatures by RF magnetron sputtering technique, and (c) a comparison between the variations in crystalline micro-strains (for main diffraction orientation (104)) and phonon lifetimes (for 416 cm⁻¹ Raman peak).

Sample	2θ ₍₁₀₄₎ (°)	FWHM XRD (°)	D(nm)	δ (× 10 ⁻³ nm ⁻²)	ε (× 10 ⁻³)	FWHM Raman (cm ⁻¹)
T25	37.60	0.96	9.13	12.02	3.97	13.82
T100	37.52	0.96	9.14	12.00	3.96	13.04
T200	37.35	0.60	14.62	4.68	2.48	11.85
T300	37.60	0.72	12.19	6.72	2.97	22.87

Table 3. Crystallographic parameters of the samples, based on the main diffraction orientation (104) and Raman FWHM for 416 cm⁻¹ peak.

$$\frac{1}{\tau} = \frac{\Delta E}{\hbar} = 2\pi C\Gamma \quad (6)$$

Where \hbar is Planck's constant, ΔE is the uncertainty in the energy, and Γ is equal to FWHM of Raman peaks in units of cm⁻¹. According to Fig. 3c, the lifetime of phonons for samples T25, T100, T200, and T300 is 0.38, 0.40, 0.45 and 0.23 ps for 416 cm⁻¹ respectively. In the T200 sample, larger crystal size and fewer defects enhance the phonon distribution and extend the phonon lifetime³⁶. The presence of fewer defects allows for less scattering of phonons and leads to longer phonon lifetimes³⁸. This important phenomenon can help improve thermal and electrical properties and make materials more suitable for various applications. According to Table 3, it can be seen that the FWHM of peak 416 cm⁻¹ decreased with increasing temperature from 25 °C to 100 °C and then

200 °C, and at 300 °C the FWHM increased again. Raman peaks related to the WS_2 layer in T200 are sharper and stronger than other samples, which indicates a higher degree of crystallinity. The absence of additional peaks in Raman shows the purity level of the measured sample, which aligns well with the XRD analysis results for these samples³⁹.

Optical properties

Figure 4 shows the transmission and absorption spectra of all samples at wavelengths of 300–1100 nm. The average transmission in the wavelengths of 800–1100 nm for samples is 65–80% and optical reflection (5–30%) in this region. The absorption spectrum of the samples indicates that as the temperature increases, the absorption edge of the samples changes and affects their band gap. Although roughness increases with increasing substrate temperature, the observed decrease in light transmission for the T200 sample is not only due to photon scattering but also to the significant transformation of the nanosheet structures in this sample, which increases the surface-to-volume ratio. This morphological change is likely to have a more substantial impact on light transmission than roughness alone.

The optical band gaps (E_g) were calculated from the absorbance spectra of the thin films using Tauc's relation^{1,40,41}:

$$(ah\nu)^2 = A(h\nu - E_g) \quad (7)$$

The E_g values were determined by extrapolating the linear portion of the plot to the energy axis, where, $(ah\nu)^2 = 0$ ^{42,43}. The results (Fig. 5(a-d)) show that the optical band gap of samples T25, T100, T200, and T300 are 2.63, 2.38, 2.35, and, 2.39 eV respectively. According to Fig. 5(e), there is a significant relationship between the crystal size of the samples and their optical band gaps. In particular, samples with larger crystal sizes have smaller band gaps. This phenomenon can be attributed to quantum confinement effects, which occur when the dimensions of matter approach the Bohr exciton radius. As the crystal size increases, the quantum confinement effects decrease, leading to a narrowing of the energy band gap.

Electrical properties

Room temperature Hall effect measurements were performed to investigate the electrical properties of WS_2 thin films at different substrate temperatures. The results obtained, including resistivity, carrier density, and mobility, are summarized in Table 4. Increasing the substrate temperature from 25 °C to 100 °C resulted in a decrease in both carrier concentration and mobility, resulting in a significant increase in resistivity. This behavior suggests enhanced charge scattering, likely due to the emergence of microstructural irregularities or localized defects. At T200, the resistance increases, and the carrier density and mobility decrease dramatically. This can be attributed to the increased carrier dispersion due to the formation of grain boundaries, nanosheets, and higher porosity. Although the crystalline structure is still evident in the XRD patterns, the dominant effect seems to be related to structural disorder and high porosity, which lead to strong phonon scattering and carrier trapping, ultimately reducing the conductivity. At T300, the electrical properties improved again, with a decrease in resistance and an increase in carrier density and mobility. This change could be due to structural rearrangement in which nanoparticles are more uniformly distributed and carrier scattering is reduced. These results indicate that substrate temperature plays a key role in tuning the electrical properties of WS_2 films, and to fully understand the charge transport behavior, one must consider the complex interplay between microstructure, crystal order, and surface porosity.

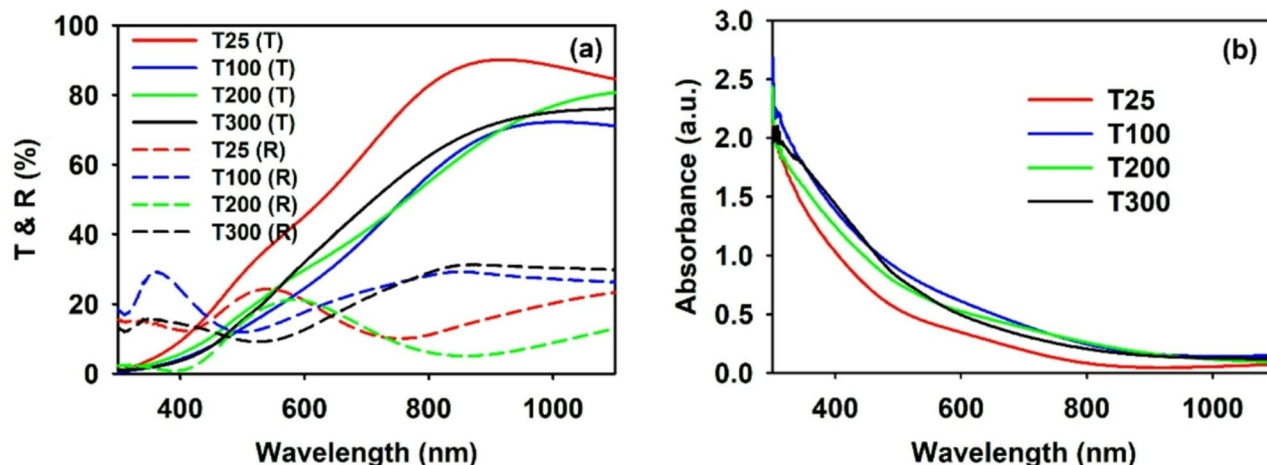


Fig. 4. (a) Transmittance and reflectance spectra; (b) Absorbance spectra for WS_2 thin films deposited at various temperatures by RF sputtering technique.

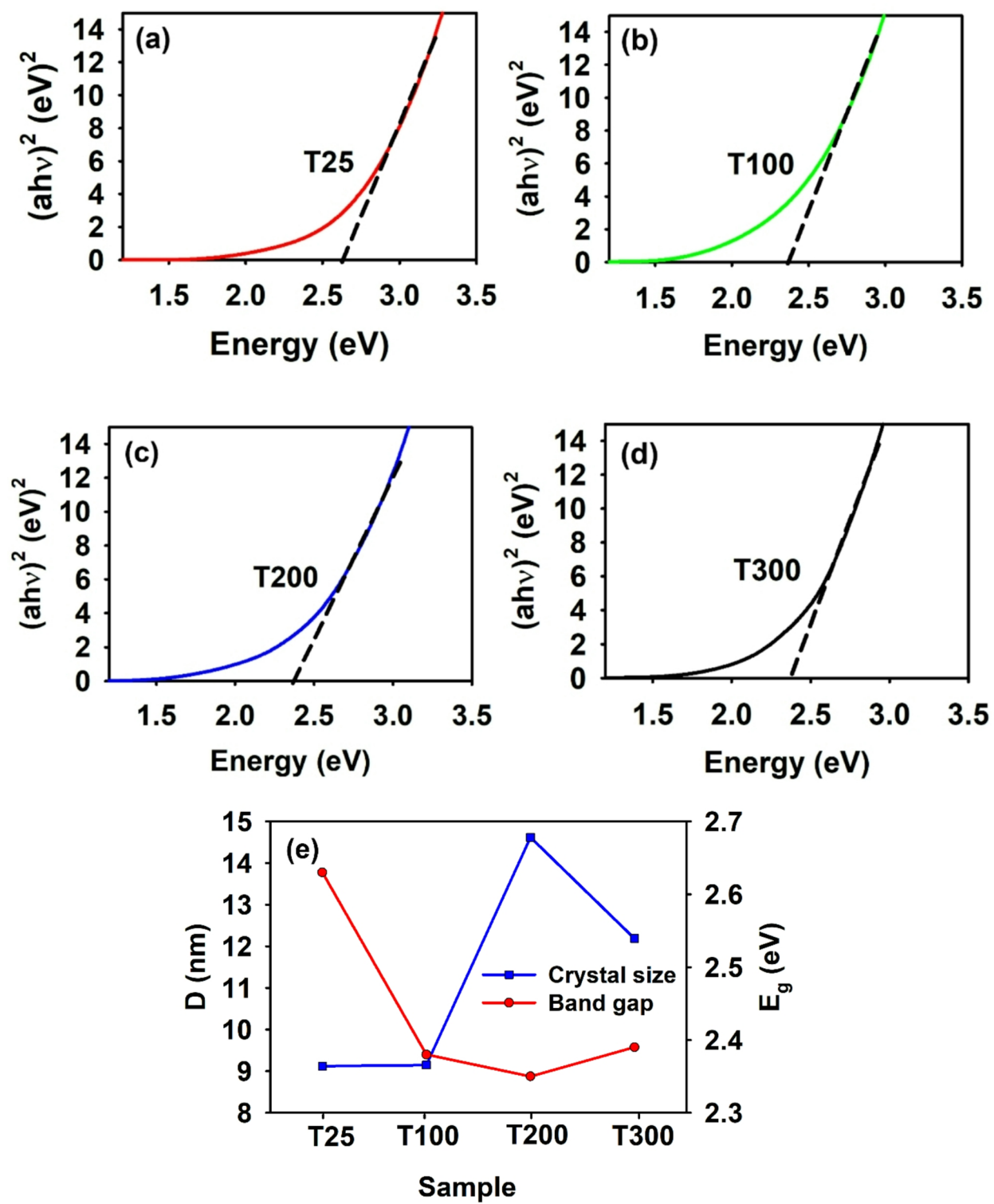


Fig. 5. (a-d) The estimation E_g of WS_2 prepared at various substrate temperatures, (e) Comparison between crystalline size and band gap energy for WS_2 samples deposited at various temperatures by RF magnetron sputtering method.

Conclusion

In this study, WS_2 thin films were deposited onto glass substrates using RF magnetron sputtering with a WS_2 target. The influence of substrate temperature was investigated on the morphological, structural, and optical properties of the WS_2 thin films. The FESEM images showed that all the deposited samples had a constant thickness of about 200 nm. Notably, the T200 sample shows a unique morphology with a series of nanosheets.

Sample	Resistivity ($\Omega \cdot \text{cm}$)	Conductivity ($\Omega \cdot \text{cm}$) $^{-1}$	Carrier Concentration (cm^{-3})	Mobility ($\text{cm}^2/\text{V} \cdot \text{s}$)
T25	5.89	2.56×10^{-1}	5.77×10^{16}	1.71×10^2
T100	3.48×10^1	3.19×10^{-2}	8.22×10^{15}	2.42×10^1
T200	4.16×10^2	5.03×10^{-3}	1.94×10^{14}	1.02×10^{-3}
T300	4.59	2.81×10^{-1}	2.81×10^{16}	7.70×10^1

Table 4. Hall effect measurement results of the samples.

The formation of these nanosheets can increase the surface-to-volume ratio of the material and potentially improve its functional properties. The AFM spectrum shows more roughness in the T200 sample and confirms the FESEM images of the samples. Structural analysis using XRD confirmed the formation of a hexagonal WS_2 phase in all samples. The XRD analysis indicated that the film formed at a substrate temperature of 200 °C has a greater crystal size, better crystallinity, and reduced micro-strains compared to the other samples. The Raman results showed that the T200 sample has better crystallinity and a longer phonon lifetime, which aligns with the observations made through XRD analysis. It was evaluated by examining the optical properties of the band gap, and it showed that the band gap of the T200 sample was lower than other samples. This narrowing of the band gap, combined with the observed growth in crystal size, could indicate the quantum confinement effect. Regarding the electrical properties, the highest resistance was observed at 200 °C. These changes at higher temperatures were observed due to structural disorder and increased porosity, which led to greater phonon scattering and reduced electrical conductivity. In general, our findings highlight the significant influence of substrate temperature on the morphological, structural, optical, and electrical properties of the thin films. Considering the unique nanosheet-like morphology, high surface roughness, and favorable optical and electrical properties, the WS_2 thin film deposited at 200 °C could be promising for future applications in gas sensing devices.

Data availability

The datasets used and analyzed during the current study available from the corresponding author on reasonable request.

Received: 10 January 2025; Accepted: 24 June 2025

Published online: 01 July 2025

References

1. Dalouji, V., Abbasi, P. & Rahimi, N. Effect of annealing temperature on photoluminescence spectra, gap States using different models and optical dispersion parameters in copper-doped ZnO films. *Mol. Simul.* **46**, 1542–1549 (2020).
2. Wang, Q. H., Kalantar-Zadeh, K., Kis, A., Coleman, J. N. & Strano, M. S. Electronics and optoelectronics of two-dimensional transition metal dichalcogenides. *Nat. Nanotechnol.* **7**, 699–712 (2012).
3. Ma, Y. et al. Electronic and magnetic properties of perfect, vacancy-doped, and nonmetal adsorbed MoSe 2, mte 2 and WS 2 monolayers. *Phys. Chem. Chem. Phys.* **13**, 15546–15553 (2011).
4. Koppens, F. et al. Photodetectors based on graphene, other two-dimensional materials and hybrid systems. *Nat. Nanotechnol.* **9**, 780–793 (2014).
5. Li, X., Li, X., Li, Z., Wang, J. & Zhang, J. WS2 nanoflakes based selective ammonia sensors at room temperature, *Sens. Actuators B Chem.* **240**, 273–277 (2017).
6. Gao, W. et al. 2D WS2 based asymmetric Schottky photodetector with high performance. *Adv. Electron. Mater.* **7**, 2000964 (2021).
7. Pawbake, A. S., Waykar, R. G., Late, D. J. & Jadkar, S. R. Highly transparent wafer-scale synthesis of crystalline WS2 nanoparticle thin film for photodetector and humidity-sensing applications. *ACS Appl. Mater. Interfaces.* **8**, 3359–3365 (2016).
8. Cong, C. et al. Synthesis and optical properties of large-area single-crystalline 2D semiconductor WS2 monolayer from chemical vapor deposition. *Adv. Opt. Mater.* **2**, 131–136 (2014).
9. Yörulmaz, B. et al. CVD growth of monolayer WS2 through controlled seed formation and vapor density. *Mater. Sci. Semicond. Process.* **93**, 158–163 (2019).
10. Koçak, Y., Akaltun, Y. & Gür, E. Magnetron sputtered WS2; optical and structural analysis, *Journal of Physics: Conference Series* **707** 012028. (2016).
11. Akhtaruzzaman, M. et al. Impact of ar flow rates on micro-structural properties of WS2 thin film by RF Magnetron sputtering. *Nanomaterials* **11**, 1635 (2021).
12. Hankare, P. et al. WS2 thin films: Opto-electronic characterization. *J. Alloys Compd.* **479**, 657–660 (2009).
13. Kumar, A. et al. Structural and Optical Properties of Chalcogenide WS2 Thin Film, International Conference on Advanced Functional Materials and Devices 267–274. (2023).
14. Vattikuti, S. P., Byon, C. & Chitturi, V. Selective hydrothermally synthesis of hexagonal WS2 platelets and their photocatalytic performance under visible light irradiation. *Superlattices Microstruct.* **94**, 39–50 (2016).
15. Cao, S. et al. Hydrothermal synthesis of variety low dimensional WS2 nanostructures. *Mater. Lett.* **129**, 205–208 (2014).
16. Ferhati, H., Djeffal, F., Benhaya, A. E. & Bendjerad, A. Giant detectivity of ZnO-based self-powered UV photodetector by inserting an engineered back gold layer using RF sputtering. *IEEE Sens. J.* **20**, 3512–3519 (2019).
17. Ferhati, H., Bendjerad, A., Djeffal, F., Benhaya, A. & Saidi, A. Multispectral photodetection using low-cost sputtered nio/ag/ito heterostructure: from design concept to elaboration. *Ceram. Int.* **47**, 15703–15709 (2021).
18. Kang, S. J. & Joung, Y. H. Influence of substrate temperature on the optical and piezoelectric properties of ZnO thin films deposited by RF Magnetron sputtering. *Appl. Surf. Sci.* **253**, 7330–7335 (2007).
19. Li, X. Y. et al. Effect of substrate temperature on the structural and optical properties of ZnO and Al-doped ZnO thin films prepared by Dc Magnetron sputtering. *Opt. Commun.* **282**, 247–252 (2009).
20. Chaabouni, F., Abaab, M. & Rezig, B. Effect of the substrate temperature on the properties of ZnO films grown by RF Magnetron sputtering. *Mater. Sci. Eng. B.* **109**, 236–240 (2004).
21. Genut, M., Margulis, L., Tenne, R. & Hodes, G. Effect of substrate on growth of WS2 thin films. *Thin Solid Films.* **219**, 30–36 (1992).
22. Ye, W., Du, P., Xiao, S. & Li, M. Effect of annealing temperature on properties of WS2 thin films. *Surf. Eng.* **38**, 411–416 (2022).

23. Ma, S. M., Moon, J., Kwon, S. J. & Cho, E. S. Effects of DC sputtering power and rapid thermal processing temperature on tungsten disulfide (WS₂) thin films. *Mol. Cryst. Liq. Cryst.* **676**, 105–113 (2018).
24. Karabacak, T. Thin-film growth dynamics with shadowing and re-emission effects. *J. Nanophotonics.* **5**, 052501–052501 (2011).
25. Pelliccione, M., Karabacak, T., Gaire, C., Wang, G. C. & Lu, T. M. Mound formation in surface growth under shadowing. *Phys. Rev. B Condens. Matter Mater. Phys.* **74**, 125420 (2006).
26. Chalana, S. & Pillai, V. M. Substrate dependent hierarchical structures of RF sputtered ZnS films. *Appl. Surf. Sci.* **440**, 1181–1195 (2018).
27. De Oliveira, R., Albuquerque, D., Cruz, T., Yamaji, F. & Leite, F. Measurement of the nanoscale roughness by atomic force microscopy: basic principles and applications, Atomic force microscopy-imaging, measuring and manipulating surfaces at the atomic scale **3** (2012).
28. Shahidi, M., Ehsani, M., Rezagholipour Dizaji, H. & Ghazi, M. Effect of silver, gold, and platinum substrates on structural and optical properties of Tilted nanocolumnar SnS films. *J. Mater. Sci. Mater. Electron.* **31**, 2030–2039 (2020).
29. Prasad, N. & Karthikeyan, B. Resonant and Off-Resonant phonon properties of wurtzite ZnS: effect of morphology on Fröhlich coupling and phonon lifetime. *J. Phys. Chem. C* **122**, 18117–18123 (2018).
30. Al-Hardan, N. et al. A wide-band UV photodiode based on n-ZnO/p-Si heterojunctions. *Sens. Actuators A: Phys.* **207**, 61–66 (2014).
31. Tsay, C. Y., Cheng, H. C., Tung, Y. T., Tuan, W. H. & Lin, C. K. Effect of Sn-doped on microstructural and optical properties of ZnO thin films deposited by sol-gel method. *Thin Solid Films.* **517**, 1032–1036 (2008).
32. Muchuweni, E., Sathiraj, T. & Nyakotyo, H. Effect of gallium doping on the structural, optical and electrical properties of zinc oxide thin films prepared by spray pyrolysis. *Ceram. Int.* **42**, 10066–10070 (2016).
33. Ahmad, H. et al. Post-deposition annealed MoO₃ film based high performance MSM UV photodetector fabricated on Si (100). *Ceram. Int.* **46**, 20477–20487 (2020).
34. Li, H., Huang, J., Zheng, Q. & Zheng, Y. Flexible ultraviolet photodetector based ZnO film sputtered on paper. *Vacuum* **172**, 109089 (2020).
35. Kim, B. H., Kwon, S. H., Gu, H. H. & Yoon, Y. J. Negative photoconductivity of WS₂ nanosheets decorated with Au nanoparticles via electron-beam irradiation. *Phys. E Low Dimens Syst. Nanostruct.* **106**, 45–49 (2019).
36. Paul, S. & Choudhury, A. Investigation of the optical property and photocatalytic activity of mixed phase nanocrystalline Titania. *Appl. Nanosci.* **4**, 839–847 (2014).
37. Mali, S. S., Betty, C. A., Bhosale, P. N. & Patil, P. S. Hydrothermal synthesis of rutile TiO₂ with hierarchical microspheres and their characterization. *CrystEngComm* **13**, 6349–6351 (2011).
38. Wang, D., Zhao, J., Chen, B. & Zhu, C. Lattice vibration fundamentals in nanocrystalline anatase investigated with Raman scattering. *J. Phys. Condens. Matter.* **20**, 085212 (2008).
39. Zhang, J. et al. Excellent near-infrared response performance in p-CuS/n-Si heterojunction using a low-temperature solution method. *Surf. Interfaces.* **26**, 101430 (2021).
40. Zeng, X., Zhukova, M., Faniel, S., Proost, J. & Flandre, D. Structural and Opto-electronic characterization of CuO thin films prepared by DC reactive Magnetron sputtering. *J. Mater. Sci. Mater. Electron.* **31**, 4563–4573 (2020).
41. Gu, P., Zhu, X. & Yang, D. Effect of annealing temperature on the performance of photoconductive ultraviolet detectors based on ZnO thin films. *Appl. Phys. A.* **125**, 50 (2019).
42. Tang, P., Li, B. & Feng, L. The optical and electrical properties of ZnO: Al thin films deposited at low temperatures by RF Magnetron sputtering. *Ceram. Int.* **44**, 4154–4157 (2018).
43. Alkhayatt, A. H. O. et al. Low annealing temperature effect on Structural, and optical properties of CuO nanostructure thin films, IOP Conference Series: Materials Science and Engineering **871** 012094. (2020).

Acknowledgements

This research was supported by "Iran, Semnan, Semnan University" under grant number 326/1403/T140329.

Author contributions

Monireh Jafari: Conceptualization, methodology, and drafting the manuscript. Monireh led the research design and was instrumental in developing the study framework. Mohammad Mahdi Shahidi: Data collection and statistical analysis. Mohammad was responsible for gathering the research data and performing the statistical assessments. Mohammad Hossein Ehsani: Editing the manuscript. Mohammad conducted editing and refinement of the manuscript. All authors: Reviewed and approved the final version of the manuscript.

Declarations

Competing interests

The authors declare no competing interests.

Additional information

Correspondence and requests for materials should be addressed to M.M.S. or M.H.E.

Reprints and permissions information is available at www.nature.com/reprints.

Publisher's note Springer Nature remains neutral with regard to jurisdictional claims in published maps and institutional affiliations.

Open Access This article is licensed under a Creative Commons Attribution-NonCommercial-NoDerivatives 4.0 International License, which permits any non-commercial use, sharing, distribution and reproduction in any medium or format, as long as you give appropriate credit to the original author(s) and the source, provide a link to the Creative Commons licence, and indicate if you modified the licensed material. You do not have permission under this licence to share adapted material derived from this article or parts of it. The images or other third party material in this article are included in the article's Creative Commons licence, unless indicated otherwise in a credit line to the material. If material is not included in the article's Creative Commons licence and your intended use is not permitted by statutory regulation or exceeds the permitted use, you will need to obtain permission directly from the copyright holder. To view a copy of this licence, visit <http://creativecommons.org/licenses/by-nc-nd/4.0/>.

© The Author(s) 2025